ADVANCED MATERIALS INTERFACES
www.advmatinterfaces.de

Anisotropic Sliding Behaviors of Gas Bubbles upon Ferrofluid-Infused Orthonormal Tracks (FOTs) Under Magnetic Stimuli

Yucheng Bian, Suwan Zhu, Chunyang Ye, Chao Chen, Bing Xu, Yiyuan Zhang, Cong Zhang, Xinghao Wang, Yanlei Hu, Jiawen Li, Dong Wu, and Jiaru Chu*

Manipulating gas bubbles in aqueous environment exhibits both scientific and technological significance in pressure sensors, mineral flotation, and sewage disposal. Recently, the emerging ferrofluid liquid-infused porous surfaces (FLIPS) with excellent bubble magnetism-responsive functions have attracted great attention. Although current studies have focused on the isotropic bubble motion on FLIPS, the dynamic bubble slipping behaviors on anisotropic FLIPS has not been clarified yet. Herein, a kind of ferrofluid-infused orthonormal tracks (FOTs) with periodic micro-grooved structures by one-step femtosecond laser ablation is reported, exhibiting anisotropic slipping behaviors of underwater bubbles along two orthogonal directions on FOTs. Further investigation suggests that the bubble slipping distance, that is, the interfacial resistance, is subject to the ferrofluid infusion and the external driving velocities. It is revealed that the disparity of slipping resistance is mainly related to the interfacial dissipation and the anisotropic menisci reshaped by magnetic stimuli along two orthonormal directions of FOTs. Finally, relying on the anisotropic slipping motion of gas bubbles, typical applications including bubble screening and bubble-assisted optical shutter are demonstrated. This study should provide new insight into bubble slipping dynamics on lubricant-infused surfaces and prompt the development of optofluidics.

1. Introduction

The flexible manipulation of gas bubbles in aqueous media is of vital importance in both academic research and industrial settings, such as sewage disposal,[1–4] mineral flotation,[5,6] pressure sensors,[7] and gas-related electrochemistry.[8–10] To date, most of the reported approaches for manipulating gas bubbles mainly rely on the assistance of buoyancy force or the cooperation of the gradient of Laplace pressure stemming from substrate's asymmetric geometric structures.[11–15] For instance, inspired by the directional water droplet transport ability of cactus spines, Yu et al. reported a kind of superhydrophobic copper cone composed of low-surface-tension coatings capable of transporting gas bubbles along the directions of both buoyancy and anti-buoyancy due to the giant Laplace pressure difference.[16] Zhang and co-workers fabricated various superhydrophobic polymethyl methacrylate (PMMA) sheets including five-pointed star, triangle, circular, and ellipse by utilizing the techniques of laser cutting and surface superhydrophobic coating for underwater bubble management.[17]

Recently, another emerging category proposed by researchers is assigned to bio-inspired slippery liquid-infused porous surfaces (SLIPS),[18] exhibiting exceptional repellent ability toward foreign liquids and strong bubble adhesion with small resistance forces in aqueous environments.[19–22] For instance, Wang et al. fabricated lubricated geometry-gradient surfaces for anti-buoyancy bubble transport.[23] Going further, SLIPSs were also developed to achieve smart control of drops and bubbles in response to external stimuli such as temperature,[24,25] light,[26,27] and magnetic fields.[20,28] For example, Aizenberg and co-workers developed a type of hierarchical magnetism-responsive composite surface by infusing ferrofluid into a microstructured matrix, termed ferrofluid-containing liquid-infused porous surfaces (FLIPSs).[29] The magnetism-responsive FLIPSs show the excellent abilities to manipulating droplet clusters such as controlled formation, switchable and directional adhesion. Zhu et al. reported a kind of ferrofluid-infused laser-ablated microstructured

Y. Bian, S. Zhu, C. Ye, Y. Zhang, C. Zhang, X. Wang, Y. Hu, J. Li, D. Wu, J. Chu
CAS Key Laboratory of Mechanical Behavior and Design of Materials
Key Laboratory of Precision Scientific Instrumentation of Anhui Higher Education Institutes
Department of Precision Machinery and Precision Instrumentation
University of Science and Technology of China
Hefei 230026, P. R. China
E-mail: suwanzhu@ustc.edu.cn

C. Chen
College of Materials Science and Engineering
Hefei University of Technology
Hefei 230026, P. R. China

B. Xu
School of Mechanical Engineering
Suzhou University of Science and Technology
Suzhou 215009, P. R. China

The ORCID identification number(s) for the author(s) of this article can be found under https://doi.org/10.1002/admi.202102116.

DOI: 10.1002/admi.202102116

Table 1. Comparison of diverse bubble manipulation approaches.

Platform	Motion directivity	Motion dimensionality	Actuation force/mode	Maximum velocity	Anisotropic sliding	Ref.
Slippery surfaces	Bidirectional	2D	Buoyancy	≈80 cm s^{-1} tilt surface (0.02 µL bubble)	No	[19]
Slippery cones	Unidirectional	2D	Laplace force	≈90 mm s^{-1} horizontal (9 µL bubble)	No	[31]
Slippery gel surfaces	Bidirectional	2D	Buoyancy	Not mentioned	No	[20]
Slippery Fe_3O_4-doped Surfaces	Arbitrary Direction	2D	Asymmetric Laplace force	≈0.3 mm s^{-1} horizontal (2 µL bubble)	No	[32]
This work	Bidirectional	2D	Magnetic force	≈35 mm s^{-1} horizontal (5 µL bubble)	Yes	

surfaces that exhibit ultrafast horizontal bubble transport performance by taking advantage of this fast magnetism-responsive SLIPS.[30] Unfortunately, current studies mainly focus on the isotropic bubble motion on FLIPS, the dynamic behaviors of bubbles on anisotropic FLIPS have been rarely reported yet (**Table 1**). The experimental observation and explanation for bubble sliding behavior on anisotropic substrate-based FLIPSs is still lacking, which should be clarified before they can be more widely applied.

In this work, we reported a kind of ferrofluid-infused orthonormal tracks (FOTs) with anisotropic periodic micro-grooved structures through one-step femtosecond laser ablation. By regulating the amount of magnetic lubricant on the solid orthonormal tracks, we systematically investigated the anisotropic slipping behaviors of micro-bubbles on the surfaces. Our experimental results show that the anisotropic microstructures on FOTs have a great impact on the bubble slipping performance along different directions. In addition, the amount of infused ferrofluid and the driving velocity of external magnets also affect the slipping distance of bubbles. We further demonstrated that the underlying mechanism of such anisotropic slipping resistance is mainly attributed to the synergic action of the asymmetric aggregation of ferrofluid menisci and the subjacent micro-grooves along two directions. Finally, with the assistance of these anisotropic FOTs, we showed potential functions such as bubble screening and bubble-assisted optical shutter. We envision that this work should enrich the background of bubble slipping phenomena on FLIPS, and also provide technical support for related applications such as selective gaseous collection and optofluidics.

2. Results and Discussion

We fabricated FOT by choosing an aluminum sheet as the substrate for its good rust resistance in aqueous conditions. The aluminum substrate with micro-groove arrays was prepared by one-step femtosecond laser ablation. Here, we prepared two samples on two identical aluminum sheets ($30 \times 30 \times 2$ mm^3), namely sample 1 and sample 2. The sample 1 was scanned by the focused spot along the length direction and the sample 2 was the width direction (**Figure 1**a,b), the scanning speed was ≈2 mm s^{-1}. The processing area of both two samples was the same as 30×5 mm^2. The laser fabrication system and optical path can be found in Figure S1, Supporting Information. After laser ablation, the as-prepared samples were treated into superhydrophobicity with a water contact angle (WCA) >150° and then infiltrated with ferrofluid synthesized by coprecipitation method, which was elaborately described in our previous study.[30] The gas bubbles were injected directly onto the FOTs by a micro-syringe in an aqueous condition (Figure 1c).

To observe the dynamic bubble slipping behaviors on the anisotropic FOTs, we designed a bubble-driving platform. Three permanent magnets were put into a cluster under an acrylic water vessel, and the magnet cluster was placed on a mobile platform from a homemade railway system equipped with a speed-adjustable DC motor (Figure S2, Supporting Information). The typical value of the magnetic flux density (MFD) at the bubble center was measured as ≈180 mT. The driving velocity would be easily tuned by adjusting the voltages applied to the DC motor. Figure 1d shows the typical bubble slipping behaviors on FOTs under magnetic actuation, giving a significant difference in slipping distance on the two samples. The surface morphology of the two samples was observed by a scanning electron microscope (SEM). As shown in **Figure 2**, the periodic orthonormal micro-groove arrays exhibited a uniform spacing of ≈100 µm. In addition, nano-mastoids were uniformly formed on the surfaces of the micro-grooves, which were induced by the shock compression and ablation effects under the ultra-fast laser pulses.

The slipping distance of gas bubbles is one of the key indicators estimating bubble slipping resistance on functional surfaces. We quantified the influence of the infused ferrofluid volume and external driving velocity on slipping distance with different gas volumes. **Figure 3**a shows the typical snapshots of the bubble moving distances in different gas volumes (7 and 9 µL) versus the increasing ferrofluid volume and driving velocity on the two samples (see also Movie S1, Supporting Information). The detailed slipping distance of bubbles in various volumes (5, 7, 9, 11, and 13 µL) on two samples are found in Figure 3b,c, in which the driving velocity was fixed

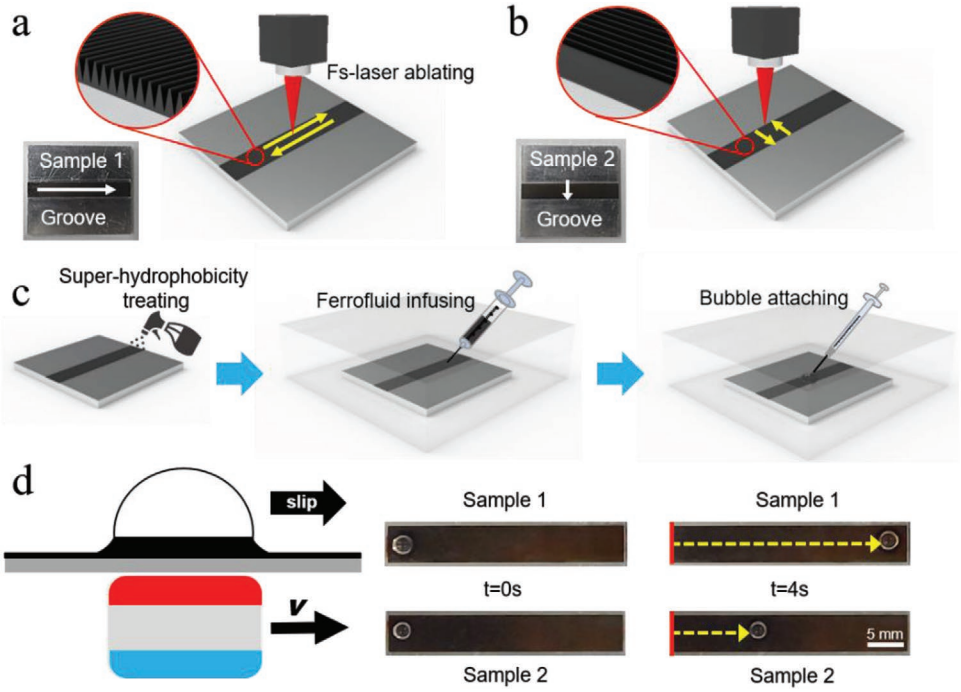

Figure 1. Schematic of the samples' fabrication via one-step femtosecond laser ablation along a) parallel and b) vertical directions of the aluminum sheets. c) Superhydrophobic treatment on the as-prepared samples. d) Schematic demonstration of the magnetism-actuated bubble slipping motion and the final distances on the two orthonormal FOTs.

at 35 mm s^{-1} and the volumes of the ferrofluid were set as 3, 5, 7, 9, and 11 µL, respectively. It can be clearly observed that for a constant driving velocity and bubble volume, the slipping distance increases with the elevation of ferrofluid amount. For instance, when the ferrofluid volume increased from 5 to 11 µL, the slipping distance of a 5 µL bubble increased from 3 to 26.8 mm on sample 1, and this similar trend was also found on sample 2, which can be ascribed to the decreased moving resistance caused by a larger amount of ferrofluid. In addition, for a fixed driving velocity and ferrofluid volume, the bubble slipping distance decreased with the increasing bubble volume as it suffered greater moving resistance.

Generally, the magnetic force exerted on the bubbles is proportional to MFD but remains difficult to be measured, as it is determined by multiple parameters (e.g., bubble size, nanoparticle concentration, etc.). We therefore employed different MFDs (120, 150, and 180 mT) to quantify their impact on bubble slipping distance on two samples with diverse Fe_3O_4/solvent mass ratios, from 1:10 to 1:30 (Figure S3, Supporting Information). The volumes of the ferrofluid and the bubbles were 7 and 9 µL, respectively. The driving velocity was 35 mm s^{-1}. It can be observed that the slipping distance increased as either MFD or Fe_3O_4/solvent mass ratio was elevated in both samples.

Figure 3d,e gives the variation of slipping distances of bubbles with increasing driving velocities in diverse ferrofluid volumes (3, 5, 7, 9, and 11 µL) on the two samples. Here the bubble volume was set as 9 µL and the driving velocities were 15, 25, 35, 50, and 60 mm s^{-1}, respectively. For a fixed bubble volume and a ferrofluid volume, the slipping distance decreased with the increasing driving velocity. Typically, when the driving velocity increased from 15 to 60 mm s^{-1}, the bubble slipping distance in 7 µL ferrofluid infusion shortened from 26.1 to 5.7 mm on sample 1, and the similar trend was also seen on sample 2, which could be attributed to the evanescent magnetic forces as the distance between the bubble and magnet cluster rapidly rose under larger driving velocities. Moreover, the increasing amount of ferrofluid resulted in a larger slipping distance, which was evidenced by Figure 3b–e. The relation between the bubble volume and the slipping distance was also quantified (Figure S4, Supporting Information). Similarly, the larger bubbles were difficult to slip far away on the FOTs, and this status could be significantly improved by the increasing amount of ferrofluid. Interestingly, we also observed that the bubble slipping distance on sample 1 was always greater than that on sample 2 in the same experimental conditions, suggesting the anisotropic bubble slipping performance along the orthonormal directions.

The anisotropic sliding velocities regarding the two samples under diverse experimental parameters were also quantified (Figure S5, Supporting Information). The time-dependent velocity data are well consistent with the motion low indicated in Figure 3. In addition, we investigated the bubble sliding behaviors on the FOTs with different groove intervals (50, 100, and 200 µm). The bubble volume was fixed at 9 µL. It can be seen that the samples with larger groove intervals exhibited lower ferrofluid volumes required to drive a static bubble (Figure S6, Supporting Information). This could be attributed to the fact that the samples with larger groove intervals retain less ferrofluid per unit area, thus more easily creating a smooth and stable ferrofluid layer under the oleoplaning bubbles. Moreover, the effect of nanostructures formed on the surfaces of micro-groove arrays on bubble sliding behaviors was briefly

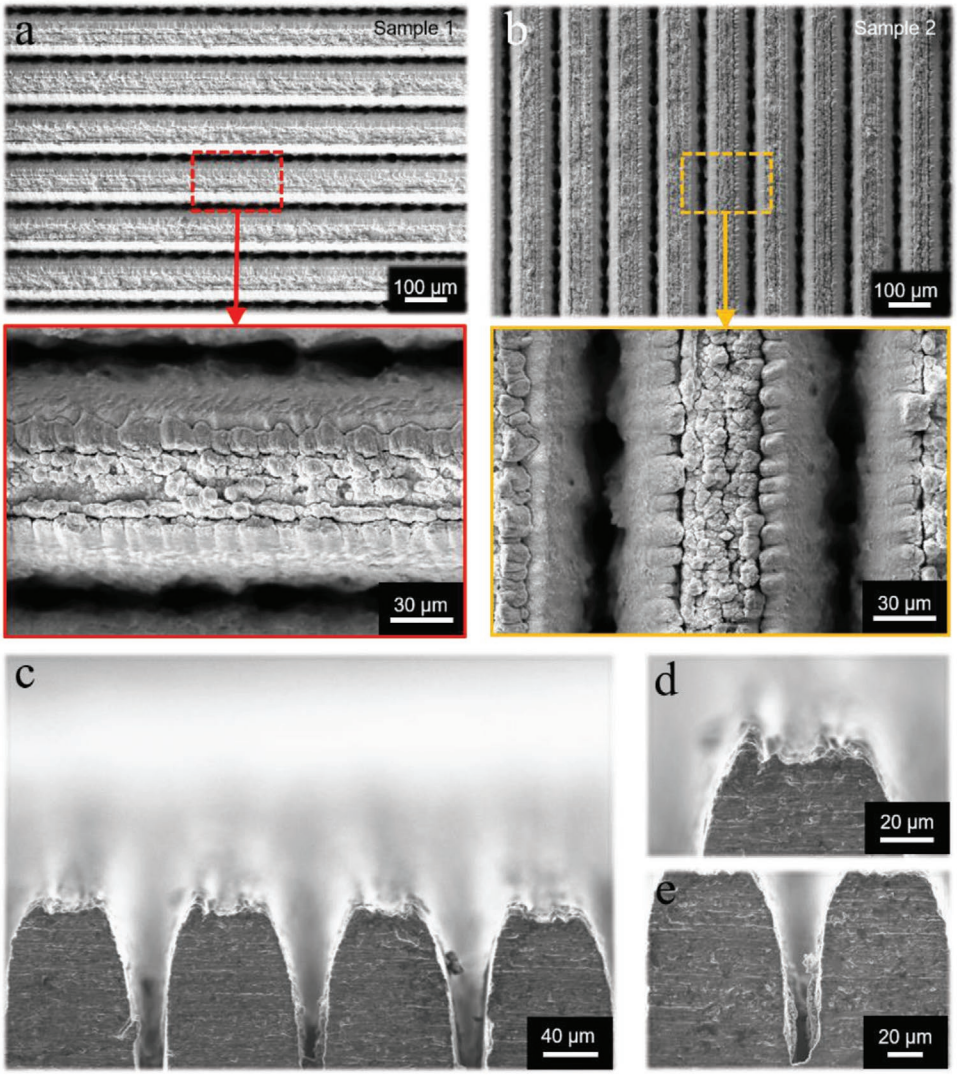

Figure 2. SEM images show the nano- and micro-grooves on the two orthonormal FOTs at different magnifications. The periodic orthonormal micro-groove arrays exhibit a uniform spacing of ≈100 μm.

discussed. We employed three samples fabricated in the same experimental conditions. The ferrofluid volume was 5 and 7 μL, respectively. The bubble volume was 9 μL. Despite the different surface nanostructures, the driving-speed-dependent slipping distances are very close along two orthonormal directions (Figure S7, Supporting Information), which suggests the negligible impact of nanostructures on bubble sliding behaviors.

To elucidate the basic physics behind the anisotropic sliding behaviors, we further focused on the detailed interfacial configurations of bubbles on the two samples. When the external magnetic field was exerted on the two FOTs, the response of ferrofluid menisci around a bubble exhibited a marked difference (**Figure 4**a). For sample 1, an elevated meniscus circle uniformly formed around a bubble. Interestingly, for sample 2, the asymmetric elevation of ferrofluid meniscus was observed, as sketched in Figure 4b. Specifically, the vertical aggregation degree of ferrofluid was less than that along the parallel direction of the micro-grooves. Such a phenomenon was merely found in sample 2, which could be simply interpreted by the fact that the longer grooves can retain more ferrofluid on sample 1, giving rise to more significant accumulation toward the bubble when the magnetic field is applied.

Generally, there are five external forces acting on an FOT-attached bubble (Figure 4c). The driving force of bubble motion is the horizontal component of the magnetic force, which is calculated as $F_{mx} = F_{magnetic} \cdot \cos \alpha$ (where α is the included angle between magnetic force and the sample surface). The total resistance in the opposite direction to the driving force is the velocity-dependent quantity $F_{drag} \approx v^k$(where k and v are the positive coefficient and bubble velocity, respectively). The buoyancy of the bubble $F_b = \rho \cdot V \cdot g$ (ρ, V, and g are water density, bubble volume, and gravitational acceleration, respectively) in the vertical direction is balanced with the adhesion force between the bubble-ferrofluid interface and the vertical component of the magnetic force $F_{my} = F_{magnetic} \cdot \sin \alpha$ from the ferrofluid. The asymmetric accumulation of ferrofluid menisci in the two samples was further evidenced by Figure 4d, in which both the ferrofluid and bubble volumes were set as 5 μL.

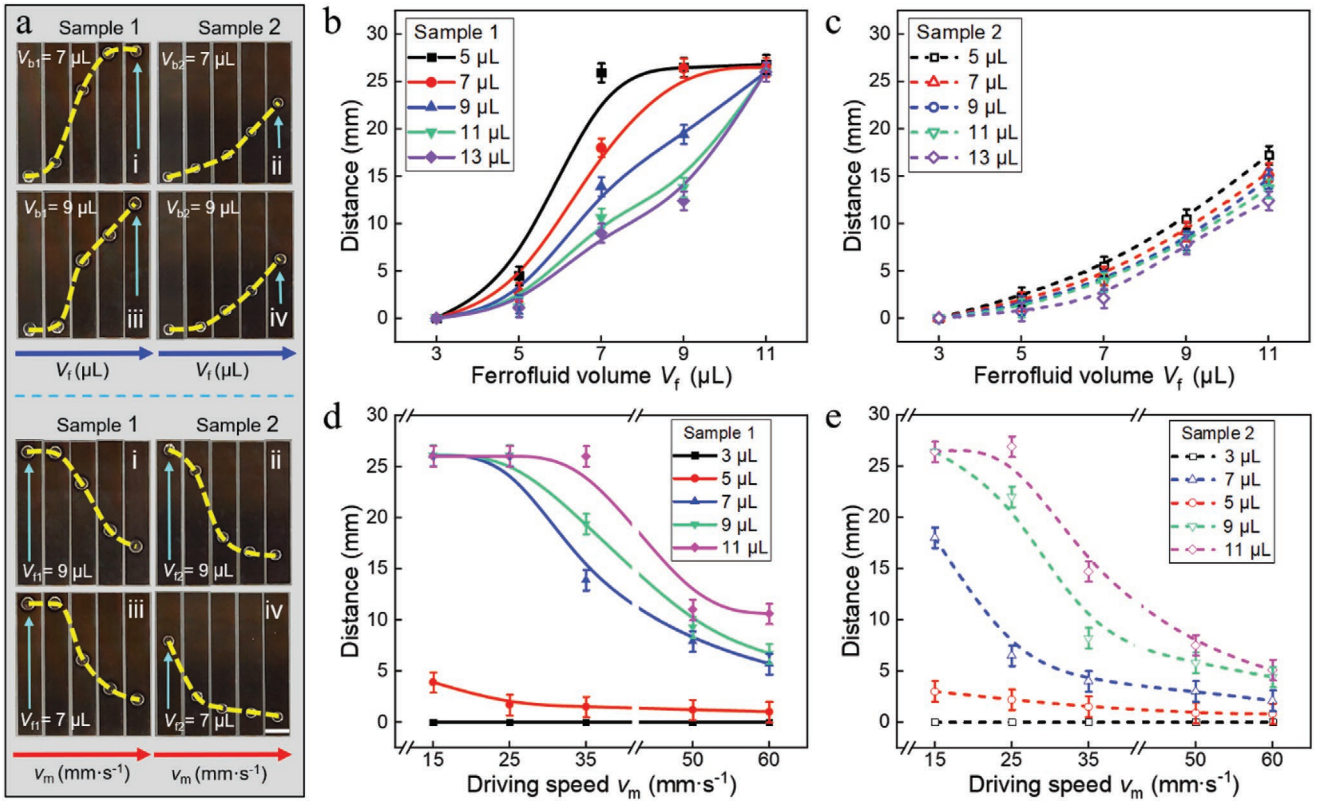

Figure 3. a) Typical snapshots of the bubble moving distances in different gas volumes (7 and 9 μL) versus the increasing ferrofluid volume and the driving velocity on the two samples. The influence of the b,c) ferrofluid volume and d,e) driving speed on the total slipping distance of bubbles in various gas volumes on the two samples. Scale bars: 5 mm.

It can be clearly observed that both the meniscus thicknesses increased significantly along the two orthonormal directions of sample 1 when the magnetic field was applied. However, for sample 2, the ferrofluid menisci only accumulated distinctly along the parallel direction of the micro-grooves.

To build the link between the slipping distance disparity and the asymmetric menisci accumulation on the FOTs, here we define six dynamical regions for a sliding bubble on a usual FLIPS, which is similar to a sliding drop on a SLIPS (Figure S8, Supporting Information).[33] Four of them concern the ferrofluid foot along the slipping direction of a moving bubble, with advancing (regions 1 and 3) and receding (regions 2 and 4) sections. The two other regions are the bubble itself (region 6) and the interface between the bubble and the FOT (region 5). Coming back to Figure 4b,d, the magnetism-reshaped ferrofluid menisci around the bubble showed markedly different along two orthonormal directions, which is the most interesting point in this work and plays a key role in the anisotropic sliding phenomena. Apparently, two distinct slippage properties were found. First, the interfacial slippages in region 5 are quite different. The longitudinal grooves provide a "fast" direction of the greatest effective slip for a slipping bubble on sample 1,[34] which endows the bubble with a minimized dissipation on the lubricant-infused grooves[35] compared to that on the latitudinal grooves on sample 2. Second, the distinct equivalent thicknesses of menisci induced by magnetic field would generate different sources of dissipation. Specifically, 1) in the case of a small amount of ferrofluid infusion ($V_m \approx 3$ μL), Landau–Levich films are not expected on the tall microstructures ($h \approx 10^2$ μm), the interfacial absorption is rather complex and is much greater than that on a more usual SLIPS, concerning the joint influence of ultra-thin oil film and the geometrical effect of microstructures. As a result, the sliding motion of bubbles could be hardly triggered (Figure 3c,d). 2) As the ferrofluid amount increases, the thickness of the magnetism-induced menisci could be equivalent to the thickness h of the microstructures. For sample 1, the raised menisci above the microstructures are found in both the advancing and receding sites. The bubble is therefore oleoplaning—akin to tires hydroplaning on a wet road—with minimal dissipative force and no contact line pinning.[36] The related frictions F_2 and F_4 scale as $2\pi(\eta_f v_b/\varepsilon)lR$, that is, $F_2 \approx 2\pi\gamma_{fw}R\mathrm{Ca}^{2/3}$ in region 2 and $F_4 \approx 2\pi\gamma_f R\mathrm{Ca}^{2/3}$ in region 4,[33] where η_f is ferrofluid viscosity, v_b is bubble velocity, ε is film thickness at the rear (region 2), l is a distance scaling as $R\mathrm{Ca}^{1/3}$, R is the bubble radius, γ_{fw} and γ_f denote the ferrofluid-water and ferrofluid-air tensions, respectively, and Ca is the capillary number $\eta_f v_b/\gamma_f$. In addition, providing the meniscus size a and a molecular size b as cutoff distances, a universal formula for the friction is given by $F_{1/3} \approx \varphi^{2/3}\ln^{2/3}(a/b)\gamma R\mathrm{Ca}^{2/3}$, with $\gamma = \gamma_f$ in region 1 and $\gamma = \gamma_{fw}$ in region 3, and φ is the pillar density within the range of 0 to 1. Conversely, for sample 2, the unrisen menisci with relatively insufficient ferrofluid along the slipping direction would result in an elevated dissipative force and contact line pinning during the bubble

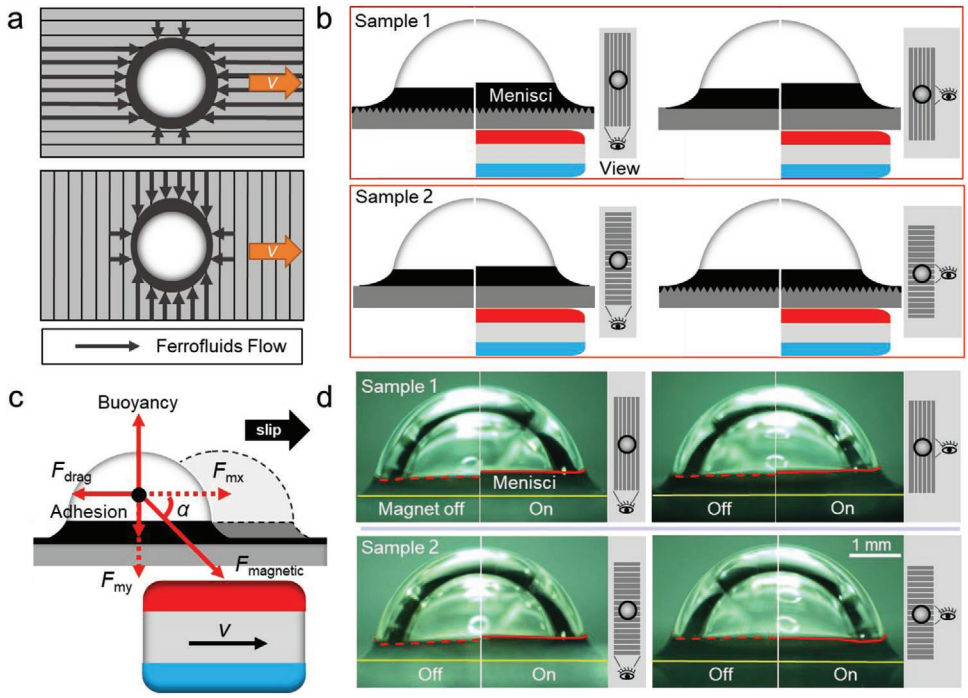

Figure 4. When external magnetic field is exerted on the two FOTs, the ferrofluid menisci around a bubble exhibit markedly different responses: Schematics of a) top view and b) side view. c) Force analysis on a magnetism-actuated bubble slipping motion. d) Photographic snapshots of the asymmetric accumulation of ferrofluid menisci induced by magnetic field on the orthonormal FOTs.

motion, giving a shorter moving distance. 3) When the FOT is over-saturated by the impregnated ferrofluid, the geometrical disparity of menisci would eventually vanish, the bubble tends to suspend inside the ferrofluid cloak, and the dissipation with similar amplitudes leads to identical distances on the two samples (Figure 3b,c). This is no longer a surface-slipping issue and is out of the scope of this study.

As analyzed above, the slipping performance of the bubbles could be effectively tuned by diverse experimental parameters including the ferrofluid infusion amount and the driving velocity on FOTs, which enables the capability of precisely controlling micro-bubbles in different volumes (**Figure 5**b, with the ferrofluid volume ≈4 µL, the driving velocity ≈15 mm s^{-1}, and the bubble volumes of 7, 9, and 11 µL from the bottom up). Accordingly, as the bubble can block the light at visible region due to the light refraction and scattering effects on the incident interfaces, we successfully realized underwater remote optical shutter and "bubble-lighting" (Figure 5a,c; Movies S2 and S3, Supporting Information) functions. The initial ferrofluid volume in each track was 3 µL and the bubble volume was 15 µL. We then increased the ferrofluid volume to 7 µL on these tracks, and the driving velocity was set as ≈15 mm s^{-1}. These demonstrations provide new potentials for various applications, such as optofluidics and all-optical modulators.

3. Conclusion

In summary, we fabricated a kind of anisotropic FOTs by utilizing one-step femtosecond laser ablation technology. This FOT possesses different geometric structure distributions in two orthonormal directions, which enables the capability of anisotropic bubble slipping behaviors on its slippery, magnetism-responsive surfaces. Our experimental results show that the anisotropic slipping motion of bubbles is related to various experimental parameters, including the amount of infused ferrofluid, external driving velocity, and the geometric configurations of anisotropic micro-grooves along the two orthogonal directions. Further analysis suggested that the underlying mechanism of such anisotropic behaviors is mainly attributed to the disparity of both interfacial dissipation and the anisotropic menisci reshaped by magnetic stimuli along two orthonormal directions of FOTs. Finally, based on the anisotropic bubble slipping phenomena, we elaborately demonstrated the potential applications such as bubble screening and bubble-assisted optical shutter. We believe that such anisotropic FOTs will enrich the physical background of the current SLIPS-based bubble control strategy, but also favor the demands in many related fields of micro-bubble management such as unidirectional gas collection and optofluidics.

4. Experimental Section

Materials: The 1060 aluminum sheets (Al, purity > 99%, 30 × 30 × 2 mm^3) were purchased from local hardware store. The Iron(II) chloride tetrahydrate ($FeCl_2$ $4H_2O$), Iron(III) chloride hexahydrate ($FeCl_3$ $6H_2O$), Ammonia solution (NH_3 H_2O, 25 wt.%), Oleic acid, and n-Octane were purchased from Sinopharm Chemical Reagent Co., Ltd. The magnets (ϕ10 × 5 mm) used in the experiment were purchased from Shanghai Ze He Mechanical & electrical co., Ltd. The superhydrophobic spray (Glaco

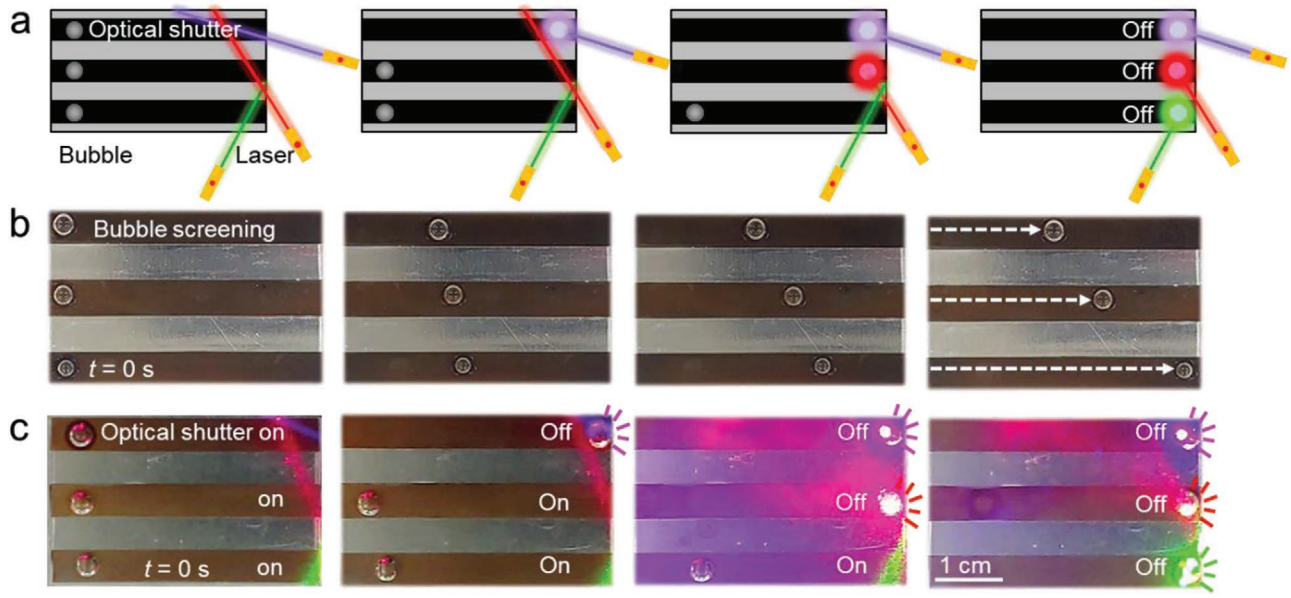

Figure 5. a) Schematic demonstration for potential application of underwater remote optical shutter. b) Snapshots of bubble screening by different bubble volumes at the same driving speed. c) Snapshots of "bubble-lighting" and underwater optical shutter. The bubble on each track was accurately transported to the light path lying at the end of the track in turn, blocking and scattering light at visible region at the incident interfaces.

Mirror Coat Zero, Soft 99 Ltd, Japan) was used to treat the laser-textured aluminum sheets, which contains silica nanoparticles (≈40 nm) and organic reagent.

Synthesis of the Ferrofluid: Iron oxide nanocrystals were synthesized with the coprecipitation method. $FeCl_3$ $6H_2O$ (5.4 g, 20 mmol) was added to a 200 mL water solution containing $FeCl_2$ $4H_2O$ (2.0 g, 10 mmol) and then stirred for 30 min. NH_3 H_2O (25 wt.%, 7 mL) was added dropwise to the mixture under vigorous stirring, resulting in the formation of Fe_3O_4 nanocrystals in weak alkaline solution. After stirring for 3 h, the resulting precipitate was isolated from the mixture with a strong magnet, washed with deionized water three times. Oleic acid (1.22 g, 4.3 mmol) was added dropwise to Fe_3O_4/ water suspension at 80 °C under nitrogen protection and continuous stirring for 30 min. Finally, the surface-modified Fe_3O_4 nanocrystals were uniformly dispersed in n-Octane (3.2 mL, 20 mmol) and ready for use. Here n-Octane was chosen to satisfy the basic criterion that the carrier fluid for iron oxide nanoparticles should be aerophilic with low viscosity and immiscible with ambient water.

Femtosecond Laser Fabrication: The laser beam (<100 fs, 1 kHz, 800 nm) from a Ti:sapphire femtosecond laser system (80L8TICEACE-100F-1K, Spectra-Physics Solstice Ace, USA) was employed to construct periodic micro-grooved structures on the aluminum sheet. Laser was focused on the aluminum surface by an f-theta lens (focal length ≈100 mm), and the preprogramed scanning path was guided by a galvo-scanner system (s-9210d, Sunny Technology, China). By controlling the laser power at 300 mW, scanning speed at 2 mm s^{-1}, and scanning repetition of 10 times, periodic micro-grooved structures can be constructed on the aluminum sheet.

Characterization: The contact angle of the water was measured with a contact-angle system (Innuo CA100C, China) by a sessile drop method. Surface morphologies of the laser-textured aluminum sheets were observed by a secondary electron SEM (Zeiss EVO18) with an accelerating voltage at 10 kV.

Supporting Information

Supporting Information is available from the Wiley Online Library or from the author.

Acknowledgements

This work was supported by the National Natural Science Foundation of China (Nos. U20A20290, 61927814, 52122511, 91963127, 52075516, 51875544, 52005475, and 62105090), Major Scientific and Technological Projects in Anhui Province (201903a05020005), and the Fundamental Research Funds for the Central Universities (Nos. WK2090000035, WK2090050048, WK2480000005, and YD2090002005). The authors acknowledge the Experimental Center of Engineering and Material Sciences at USTC for the fabrication and measuring of samples. This work was partly carried out at the USTC Center for Micro and Nanoscale Research and Fabrication.

Conflict of Interest

The authors declare no conflict of interest.

Data Availability Statement

The data that support the findings of this study are available from the corresponding author upon reasonable request.

Keywords

bubble manipulation, femtosecond laser, ferrofluid, menisci, slippery surfaces

Received: October 28, 2021
Revised: December 12, 2021
Published online: January 28, 2022

[1] M. S. Siddiqui, G. L. Amy, B. D. Murphy, *Water Res.* **1997**, *31*, 3098.
[2] H. Odegaard, *Water Sci. Technol.* **2001**, *43*, 75.

[3] T. A. Ternes, M. Meisenheimer, D. McDowell, F. Sacher, H. J. Brauch, B. Haist-Gulde, G. Preuss, U. Wilme, N. Zulei-Seibert, *Environ. Sci. Technol.* **2002**, *36*, 3855.
[4] E. Forgacs, T. Cserhati, G. Oros, *Environ. Int.* **2004**, *30*, 953.
[5] M. S. K. A. Sarkar, S. W. Donne, G. M. Evans, *Adv. Powder Technol.* **2010**, *21*, 412.
[6] P. T. L. Koh, M. Manickam, M. P. Schwarz, *Miner. Eng.* **2000**, *13*, 1455.
[7] M. J. F. Warnier, M. H. J. M. De Croon, E. V. Rebrov, J. C. Schouten, *Microfluid. Nanofluid.* **2010**, *8*, 33.
[8] Z. Y. Lu, W. Zhu, X. Y. Yu, H. C. Zhang, Y. J. Li, X. M. Sun, X. W. Wang, H. Wang, J. M. Wang, J. Luo, X. D. Lei, L. Jiang, *Adv. Mater.* **2014**, *26*, 2683.
[9] C. M. Yu, M. Y. Cao, Z. C. Dong, K. Li, C. L. Yu, J. M. Wang, L. Jiang, *Adv. Funct. Mater.* **2016**, *26*, 6830.
[10] Y. J. Li, H. C. Zhang, T. H. Xu, Z. Y. Lu, X. C. Wu, P. B. Wan, *Adv. Funct. Mater.* **2015**, *25*, 1737.
[11] X. Z. Xue, R. X. Wang, L. W. Lan, J. M. Wang, Z. X. Xue, L. Jiang, *ACS Appl. Mater. Interfaces* **2018**, *10*, 5099.
[12] S. W. Zhu, Y. C. Bian, T. Wu, E. Q. Li, J. W. Li, Y. L. Hu, D. Wu, J. R. Chu, *Appl. Phys. Lett.* **2020**, *116*, 093706.
[13] Y. Tian, B. Su, L. Jiang, *Adv. Mater.* **2014**, *26*, 6871.
[14] K. Yin, S. Yang, X. R. Dong, D. K. Chu, J. A. Duan, J. He, *Appl. Phys. Lett.* **2018**, *112*, 243701.
[15] J. A. Duan, X. R. Dong, K. Yin, S. Yang, D. K. Chu, *Appl. Phys. Lett.* **2018**, *113*, 203704.
[16] C. M. Yu, M. Y. Cao, Z. C. Dong, J. M. Wang, K. Li, L. Jiang, *Adv. Funct. Mater.* **2016**, *26*, 3236.
[17] C. H. Zhang, B. Zhang, H. Y. Ma, Z. Li, X. Xiao, Y. H. Zhang, X. Y. Cui, C. M. Yu, M. Y. Cao, L. Jiang, *ACS Nano* **2018**, *12*, 2048.
[18] T. S. Wong, S. H. Kang, S. K. Tang, E. J. Smythe, B. D. Hatton, A. Grinthal, J. Aizenberg, *Nature* **2011**, *477*, 443.
[19] C. M. Yu, X. B. Zhu, K. Li, M. Y. Cao, L. Jiang, *Adv. Funct. Mater.* **2017**, *27*, 1701605.
[20] P. Guo, Z. B. Wang, L. P. Heng, Y. Q. Zhang, X. Wang, L. Jiang, *Adv. Funct. Mater.* **2019**, *29*, 1808717.
[21] Y. L. Jiao, X. D. Lv, Y. Y. Zhang, C. Z. Li, J. W. Li, H. Wu, Y. Xiao, S. Z. Wu, Y. L. Hu, D. Wu, J. R. Chu, *Nanoscale* **2019**, *11*, 1370.
[22] X. D. Lv, Y. L. Jiao, S. Z. Wu, C. Z. Li, Y. Y. Zhang, J. W. Li, Y. L. Hu, D. Wu, *ACS Appl. Mater. Interfaces* **2019**, *11*, 20574.
[23] X. Tang, H. R. Xiong, T. T. Kong, Y. Tian, W. D. Li, L. Q. Wang, *ACS Appl. Mater. Interfaces* **2018**, *10*, 3029.
[24] X. Yao, J. Ju, S. Yang, J. J. Wang, L. Jiang, *Adv. Mater.* **2014**, *26*, 1895.
[25] C. Chen, Z. C. Huang, Y. L. Jiao, L. A. Shi, Y. Y. Zhang, J. W. Li, C. Z. Li, X. D. Lv, S. Z. Wu, Y. L. Hu, W. L. Zhu, D. Wu, J. R. Chu, L. Jiang, *ACS Nano* **2019**, *13*, 5742.
[26] J. Wang, W. Gao, H. Zhang, M. H. Zou, Y. P. Chen, Y. J. Zhao, *Sci. Adv.* **2018**, *4*, eaat7392.
[27] Z. C. Huang, C. Chen, X. H. Wang, R. Li, Y. C. Bian, S. W. Zhu, Y. L. Hu, J. W. Li, D. Wu, J. R. Chu, *ACS Appl. Mater. Interfaces* **2021**, *13*, 9272.
[28] Z. Y. Wang, R. Tao, J. Wu, B. Li, C. L. Hao, *Appl. Phys. Lett.* **2021**, *119*, 041601.
[29] W. D. Wang, J. V. I. Timonen, A. Carlson, D. M. Drotlef, C. T. Zhang, S. Kolle, A. Grinthal, T. S. Wong, B. Hatton, S. H. Kang, S. Kennedy, J. Chi, R. T. Blough, M. Sitti, L. Mahadevan, J. Aizenberg, *Nature* **2018**, *559*, 77.
[30] S. W. Zhu, Y. C. Bian, T. Wu, C. Chen, Y. L. Jiao, Z. W. Jiang, Z. C. Huang, E. Q. Li, J. W. Li, J. R. Chu, Y. L. Hu, D. Wu, L. Jiang, *Nano Lett.* **2020**, *20*, 5513.
[31] X. Xiao, C. H. Zhang, H. Y. Ma, Y. H. Zhang, G. L. Liu, M. Y. Cao, C. M. Yu, L. Jiang, *ACS Nano* **2019**, *13*, 4083.
[32] C. Chen, Z. C. Huang, L. A. Shi, Y. L. Jiao, S. W. Zhu, J. W. Li, Y. L. Hu, J. R. Chu, D. Wu, L. Jiang, *Adv. Funct. Mater.* **2019**, *29*, 1904766.
[33] A. Keiser, P. Baumli, D. Vollmer, D. Quéré, *Phys. Rev. Fluids* **2020**, *5*, 014005.
[34] M. Z. Bazant, O. I. Vinogradova, *J. Fluid Mech.* **2008**, *613*, 125.
[35] E. S. Asmolov, T. V. Nizkaya, O. I. Vinogradova, *Phys. Rev. E* **2018**, *98*, 033103.
[36] D. Daniel, J. V. Timonen, R. Li, S. J. Velling, J. Aizenberg, *Nat. Phys.* **2017**, *13*, 1020.